

Strain induced second-order Jahn-Teller reconstruction and magnetic moment modulation at monovacancy in graphene

Cite as: J. Appl. Phys. 130, 034303 (2021); doi: 10.1063/5.0050688

Submitted: 17 March 2021 · Accepted: 2 July 2021 ·

Published Online: 21 July 2021 · Publisher error corrected: 22 July 2021



View Online



Export Citation



CrossMark

Claire Andreasen, Tengyuan Hao, Julia Hatoum, and Zubaer M. Hossain^{a)}

AFFILIATIONS

Laboratory of Mechanics and Physics of Heterogeneous Materials, Department of Mechanical Engineering, University of Delaware, Newark, Delaware 19716, USA

^{a)}Author to whom correspondence should be addressed: zubaer@udel.edu

ABSTRACT

Using density functional theory simulations, we examine the electronic structure of an isolated monovacancy defect in graphene under symmetry-breaking deformation. Results show that the defect experiences a second-order Jahn-Teller reconstruction at a critical strain of 1.7%. It stabilizes the orientation of the JT bond relative to the loading direction and breaks the threefold degeneracy of the defect structure. We call it Jahn-Teller re-reconstruction (JTTR), and it is mechanically reversible. The reversibility and stabilization of the orientation depend on the direction cosine between the JT bond and the loading direction. Also, a change in the loading direction by 90° can change the orientation of the JT bond by 120°. An atomic-scale analysis suggests that the maximum bond force arising from “the derivative of the kinetic energy of electrons” defines the critical strain. JTTR alters the electron occupation in the individual electronic orbitals at the defect site. The electronic charge redistribution and the density of states at the defective sites reveal that the p_z orbitals dominate the reconstruction process. Furthermore, JTTR changes the magnitude of the magnetic moment at the defective site from $1.36\ \mu_B$ to $1.22\ \mu_B$. This unravels a new way of controlling the magnetic behavior of monovacancy by applying symmetry-breaking mechanical strain. Results also show that passivation of the dangling bond can subside or eliminate the reconstruction process depending on the number of valence electrons available in the passivating atom.

Published under an exclusive license by AIP Publishing. <https://doi.org/10.1063/5.0050688>

I. INTRODUCTION

Vacancy defects have been widely observed in graphene and other low-dimensional materials, including hexagonal boron nitride (hBN) and transition metal dichalcogenides (TMDCs).^{1,2} Monovacancy (MV) defects are a special class of vacancy defects due to their importance in electrical, thermal, and mechanical applications.^{3,4} MVs can diffuse and coalesce to form other defects as well.² One distinguishing feature of a MV in graphene is that it produces extended electronic states and imparts magnetic moment that can be as large as $1.53\ \mu_B$.^{4–13} Depending on the relative positions among a set of MV defects, the magnetic state can be either ferromagnetic or antiferromagnetic. However, controlling the magnetic moment and stabilizing the orientation of the reconstructed defect structure remain a challenge.

Likewise, defects beyond a critical distance (of around $30.0\ \text{\AA}$)¹⁴ are elastically non-interacting and the intensity of elastic interaction is strongly dependent on the direction of loading. This makes the collective properties of MV defects controllable by engineering the density and distribution of defects. The behavior of a set of MVs can be altered further, if strain is applied to the lattice and chirality-dependent features are exploited to access different directional properties. A carefully regulated array of defects can offer novel electronic and magnetic properties and functions that are unattainable from pristine graphene.^{5,15–19}

Extensive experimental and theoretical research has been conducted to determine the mechanical and electrical properties of pristine as well as wrinkled graphene under applied strain.^{20–27} It was found that localized reconstructions and associated strain fields affected the properties of the atoms surrounding the defective

site.^{28–32} Nevertheless, the magnetic implication of applied deformation for loading along an arbitrary crystallographic direction remains relatively unexplored.

The basic structure of a vacancy defect can be described as a collection of fully coordinated and partially coordinated atoms at the defective site. Both reconstructed MVs and un-reconstructed MVs have been observed experimentally in graphene.^{2,13,33,34} Variations in the number of nearest-neighbors at a defective site lead to a reconstruction of the bonds that minimize the total energy of the system. This reconstruction is denoted as the Jahn-Teller reconstruction (JTR).^{35,36} It forms a longer bond than the equilibrium bond length at the opposing end of the unsaturated atom at the defect site. Un-reconstructed MVs retain their threefold (C_3) symmetry, while the reconstructed MVs have a twofold (C_2) symmetry. The reconstruction may occur at one of the three identical sites at the defect but may switch to either of the remaining two possible degenerate defect structures at finite temperatures. Dynamic JT reconstruction can, however, change the orientation of the defect among the three possible degenerate orientations at the room temperature.^{13,37–39} This makes it difficult to control the magnetic properties in real applications. This raises the question: can defect orientation be stabilized and controlled in order to modulate the magnetic properties of the defect?

In this work, using first-principles simulations, we show that symmetry-breaking strain can play a critical role in controlling and stabilizing the orientation of a MV defect. We establish a fundamental understanding of the effects of strain on magnetic properties and stability of the structures from an electronic structure perspective. We consider four loading directions ($\theta = 0^\circ$, $\theta = 11^\circ$, $\theta = 19^\circ$, and $\theta = 30^\circ$), where θ is the chirality of the lattice, measured relative to the loading direction. We address six interrelated questions: (a) How do electrons redistribute at the defective site under different loading conditions? (b) How does the chirality affect the distribution? (c) How does symmetry-breaking at the defective site affect the localized character of the electronic states? (d) How does passivation modulate the local reconstruction at the defective site? (e) Is there a correlation between stress and electron distribution at the defective site? and (f) Is it possible to control defect magnetization by strain? Our results show that the defect orientation and magnetic moment can be controlled substantially by applying symmetry-breaking uniaxial strain. We present the paper in two primary sections: (i) simulation details and (ii) results and discussions.

II. SIMULATION DETAILS

The simulations are conducted using the open-source DFT code SIESTA.^{40–42} It uses a linear combination of atomic orbitals (LCAOs) as the approximation for the basis functions. The LCAO bases describe atomic properties in terms of the electronic character of the individual orbitals. We used the double zeta polarization (DZP) basis for the calculations. For the exchange-correlation part of electronic interactions, the generalized gradient approximation (GGA) proposed by Perdew, Burke, and Ernzerhof⁴³ is used. The core electrons of the atoms are replaced by norm-conserving pseudopotentials, following the Troullier and Martins scheme.⁴⁴ The pseudopotential for the C atom is generated by using the

$2s^2 2p^2 3d^0 4f^0$ electron configuration. The pseudopotentials for the passivating atoms, hydrogen and nitrogen, are generated using $1s^1 2p^0 3d^0 4f^0$ and $1s^2 2p^3 3d^0 4f^0$ configurations, respectively. Relativistic effects are taken into account in generating the pseudopotentials such that spin-polarization or spin-orbit coupling effects can be incorporated in the simulations. All calculations are converged for an energy cutoff of 50 meV for the basis functions and a mesh cutoff of 400.0 Ry. The selected pseudopotential, basis, mesh cutoff, and energy cutoff produce experimentally measured equilibrium elastic properties and the stress-strain curves of the lattice.⁴⁵

The simulated atomic configurations comprise N number of atoms, where $N = 127$, 167, 223, and 147 for $\theta = 0^\circ$, 11° , 19° , and 30° , respectively. The physical size of the domain within the plane ranges from $19.523 \times 18.871\text{06}\text{ \AA}^2$ for the 0° configuration to $25.889 \times 24.8996\text{ \AA}^2$ for the 19° configuration. The size-difference originates from the requirement of periodicity of the lattice that varies with the chirality of the lattice.⁴⁵ The out-of-plane dimension of the supercell is taken as 15 Å, which is sufficient to avoid the interactions of the graphene lattice with its periodic image. A Monkhorst-Pack k -mesh grid of $4 \times 4 \times 6$ consisting of 60 k -points is found to be necessary and sufficient to obtain converged stress and energy values, regardless of the deformation and defective states of the lattice. To obtain the electronic properties (the density of states and the electronic charge), a finer mesh consisting of 223 k -points is used.

The equilibrium defect structure is obtained by removing one atom from the perfect lattice and relaxing the system until a stress threshold of 0.1 GPa is achieved. Uniaxial deformation is modeled by deforming the lattice along the loading direction at a strain-rate of 0.1%. At each loading state, the domain along the lateral direction and the atomic coordinates in all directions are allowed to relax under the constraint of the imposed displacement along the loading direction. The relaxation calculations are carried out by performing a number of self-consistent field (SCF) calculations and ensuring that the system reaches a stress-tolerance of 0.1 GPa, for each of the nine stress tensor components. The system is relaxed by applying the Broyden scheme with a force tolerance of 0.01 eV/Å. Convergence of total energy is achieved with an energy threshold of 0.1 meV/atom and a force tolerance of 0.04 eV/Å. The stress tensor is computed using the Virial scheme^{46–48} as implemented in SIESTA.

The electron occupations are determined with the Mullikan Population Analysis (MPA) scheme.⁴⁹ There are several charge partitioning schemes available, such as the Bader Population Analysis (BPA),⁵⁰ the Hirshfeld Population Analysis (HPA),⁵¹ and the Natural Population Analysis (NPA).⁵² However, it is only the MPA scheme that provides an orbital-dependent decomposition scheme. In spite of the discrepancies among the schemes (in terms of how the total charge is partitioned among different atoms⁵³), the “change in electron population per atom” due to applied deformation can be deemed method-independent. Also, the “change in electron population per orbital” is a reliable estimator of the deformation-dependent electron population. It is widely used to analyze the local atomic properties for a number of bulk, molecular, and defective systems.^{5,54–56} In addition to describing chemical interactions of molecular systems, the MPA scheme is known to provide reliable mechanical properties (such as hardness in solids

with the zinc blende structure⁵⁷). We, therefore, use the MPA scheme to examine the change in electron occupation in the individual electronic orbitals. The electron density maps are generated using the XCrysden⁵⁸ and Vesta⁵⁹ software packages, and the atomic configurations showing the bond length variations in the lattice are generated using the OVITO package.⁶⁰

III. RESULTS AND DISCUSSIONS

The results and discussions are presented in two primary sections: (i) defect structure and electronic properties under the undeformed condition and (ii) defect structure and electronic properties under deformed conditions for four different chiralities of the lattice.

A. Electronic structure of undeformed monovacancy

The equilibrium defect structure of a monovacancy is displayed in Fig. 1. The length of the reconstructed bond or the JT bond, marked by *ab* in the figure, is 1.8889 Å which is within 0.5% of the experimentally measured value of 1.9 Å.^{33,61} The strain in the JT bond is 33%. The strain in the bonds formed by the atoms of the defect core with their bulk-neighbors is less than 5.48%. This suggests a rapid decay of the strain fields emanating from the

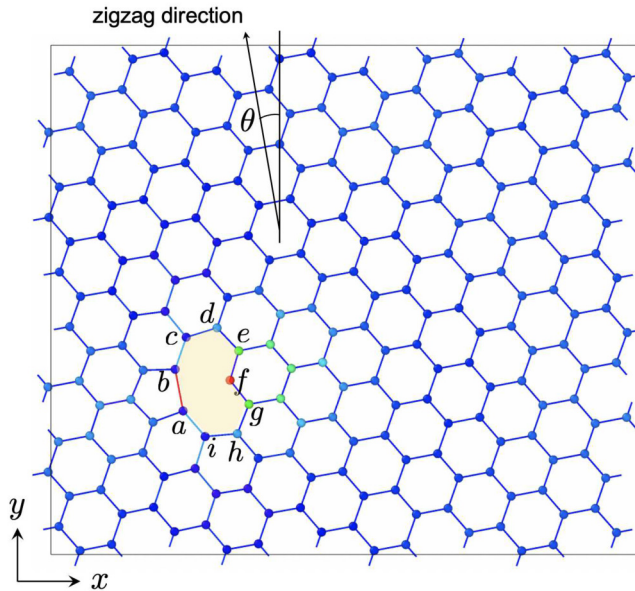


FIG. 1. Atomic configuration of the undeformed lattice of chirality $\theta = 19^\circ$, measured relative to the *y* axis. The dimensions of the supercell are 26.32 and 22.71 Å along the *x* and *y* directions, respectively. The atoms are colored according to their *z* coordinate and the bonds according to their length. The defective site *abcdefghi* is highlighted by the light-yellow surface. The bond length ranges from 1.3999 Å (of bond *ef* or *fg*) to 1.8889 Å (of bond *ab*), indicating the maximum bond length extension and contraction are 31.47% and 2.57%, respectively. The maximum out-of-plane movement of the atom at the defective site *f* is 0.294 Å. The loading direction is taken as the *y* direction.

defective site toward the bulk. As a result, the strain fields localize the redistribution of charges in the electronic orbitals of the atoms at the defect site.

For an *N*-atom graphene lattice with four orbitals (*s*, *p*_{*x*}, *p*_{*y*}, and *p*_{*z*}) per atomic site, the total charge χ is distributed over *N* numbers of *s* orbitals and $3N$ numbers of *p* orbitals. Mathematically, the partitioning can be written as a sum over the charges in the individual orbitals as:

$$\chi = \sum_{i=1}^N (\chi_i^s + \chi_i^{p_x} + \chi_i^{p_y} + \chi_i^{p_z}), \quad (1)$$

where χ_i is the charge at atom *i*. The total charge of the *N*-atom lattice is a conserved quantity and independent of the strain state of the lattice. Localized strain redistributes the charges among different orbitals. Under the undeformed state, any increase in the electronic occupation in an orbital must be accommodated by a commensurate reduction in the electron occupation in other atomic orbitals at same or neighboring atomic sites in the lattice. The defect-induced charge redistribution is, however, orbital-dependent, as exhibited in Fig. 2. Also, the redistribution process satisfies the condition that

$$\Delta\chi = \sum_{i=1}^N (\Delta\chi_i^s + \Delta\chi_i^{p_x} + \Delta\chi_i^{p_y} + \Delta\chi_i^{p_z}) = 0, \quad (2)$$

where $\Delta\chi_i$ is the change in electron occupation at atom *i*. In a defect-free lattice, the redistribution is uniform throughout the lattice. On the other hand, in a defective lattice, the electron redistribution is inhomogeneous at the defect core, but its pattern is symmetric with respect to the armchair direction passing through the defect core. The occupation in the *s*, *p*_{*x*}, and *p*_{*y*} orbitals are higher than the bulk at atomic site *f*, whereas in the *p*_{*z*} orbital, it is lower than the bulk. The atoms at sites *a* and *b* exhibit the opposite behavior. The average occupations $\int_A \chi_i(x, y) dA/N$ in the *s*, *p*_{*x*}, *p*_{*y*}, and *p*_{*z*} orbitals are 0.9807, 0.9533, 0.9167, and 0.9536, respectively. There is a clear spatial variation in the electron occupation for each of the orbitals, and the maximum and minimum occupations are different among the orbitals. For the *s*- and *p*_{*x*}-orbitals, the maximum occupations of 1.171 and 0.992, respectively, occur at the *f*-site, whereas the minimum occupation of 0.869 occurs in the *p*_{*z*}-orbital. Depletion in the *p*_{*z*}-occupation and enhancement in the *s*-occupation increases the reactivity of the *f*-site-site.

The pattern of electronic charge variations is closely related to the partial density of states (PDOS) of the atoms at the defective site. The higher electron occupation at the *f* site resulted in a large set of PDOS for the *s* orbital. Similarly, PDOS of the *p*_{*x*} and *p*_{*z*} orbitals at the *f*-site are much larger than those at other atomic sites. The direct correspondence between the PDOS and electronic charge occupation suggests an important point that the charge distribution based measure can offer insights into the available electronic states at the atomic sites. Also, the profiles of the states at the defective site depend on the tensile or compressive stress states and the number of nearest-neighbors of the atoms. The findings on electron distribution and the equilibrium defect

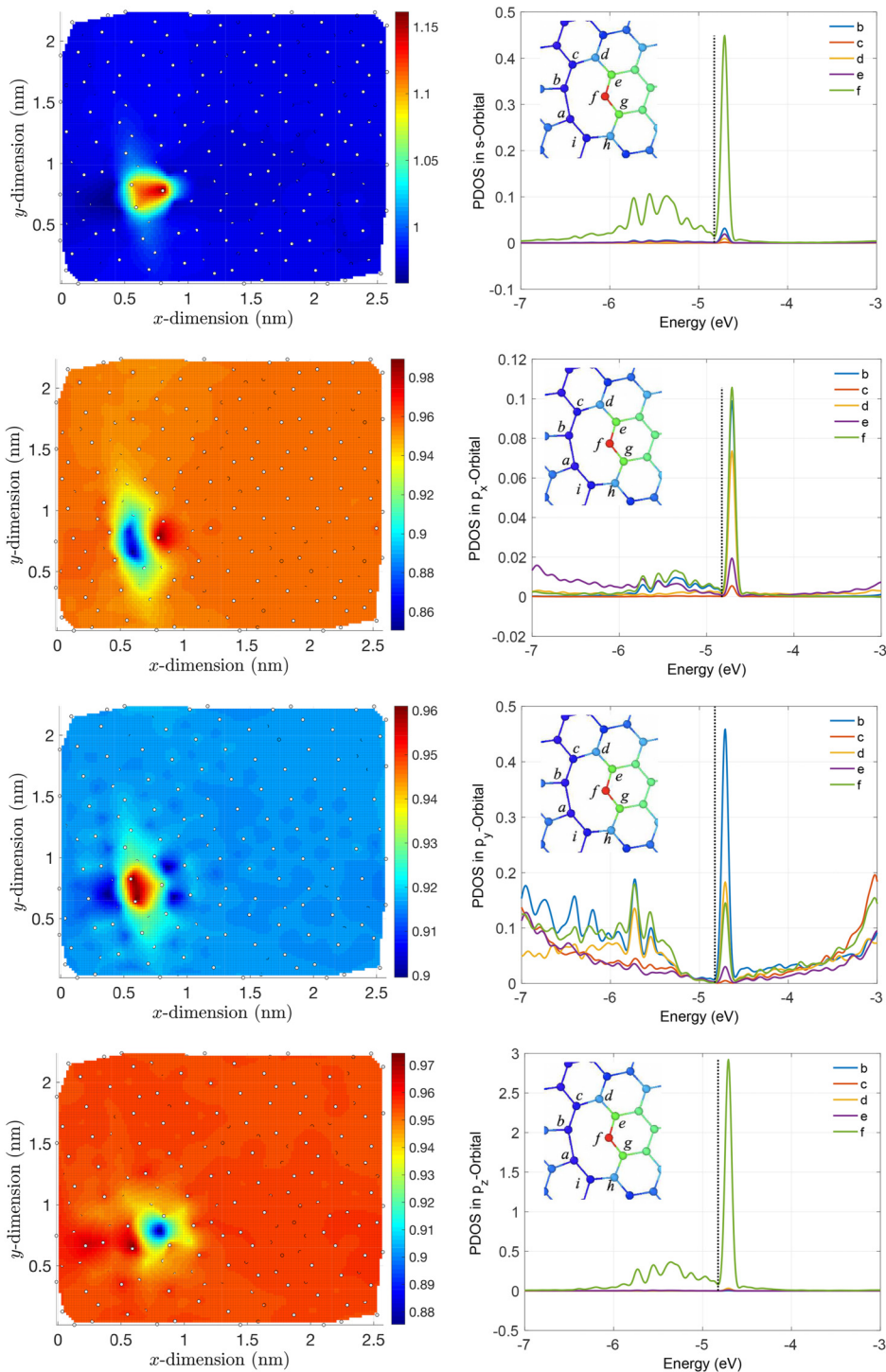


FIG. 2. A continuum scale representation of the charge distribution and partial density of states (PDOS) around the defective site in (first row) s orbital, (second row) p_x orbital, (third row) p_y orbital, and (fourth row) p_z orbital. The black circles indicate the positions of the atoms in the lattice. The PDOS of the individual orbitals surrounding the defect core are shown on the right column. Results demonstrate a direct correspondence between the orbital occupation and density of states for each orbital. The highest PDOS for the s , p_x , and p_z orbitals is observed at site f , while the highest PDOS for the p_y orbital is at site b . The dashed line indicates the armchair direction.

structure are similar for all the chiral angles. Regardless of the chirality of the lattice, the spatial variation in electron occupation and density of states can, however, be sensitive to the applied deformation.

The inhomogeneity in redistribution is centered at the f -site, which acts as the epicenter for causing the first-order and second-order Jahn-Teller reconstructions. The electronic character of the f -site can be modulated by selecting a proper chemical element or

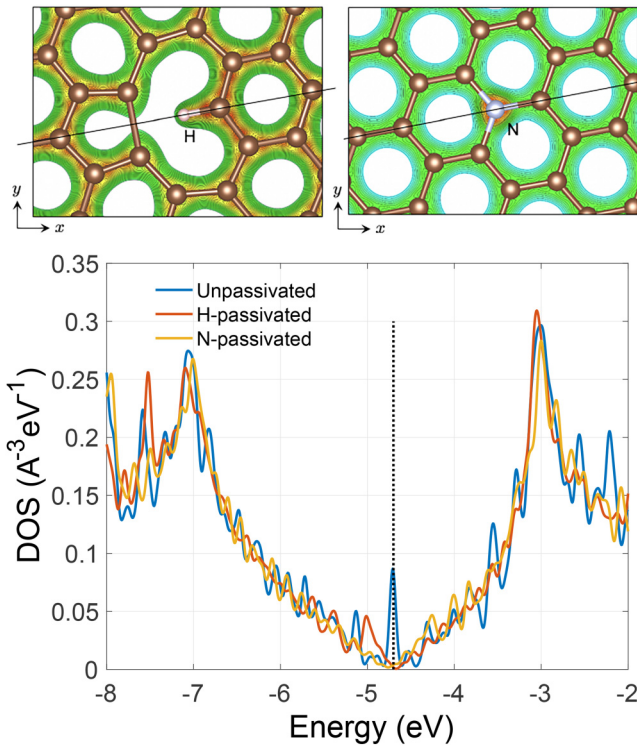


FIG. 3. Top row: (left) Hydrogen passivated defect structure and (right) N-passivated defect structure. The C–H bond length is 1.0571 Å and the longest nearest-neighbor C–C bond is 1.8802 Å at the pentagon (which is similar to what we have for the unpassivated defect structure), and the C–C bond formed at the *f* site is 1.373 Å, which is smaller than the equilibrium bond length of 1.42 Å, suggesting contraction of the C–C bond at the passivated site. Saturation of the defective site by N suppressed the out-of-plane deformation at the defective site. The presence of the N atom imposes contraction in the lattice. The solid line indicates the armchair direction with respect to which the defect structure is symmetric. (Bottom) Comparison of the total DOS for the unpassivated, H-passivated, and N-passivated cases. The Fermi energy is marked by the dashed line.

by passivating the defect. We explore this by considering two passivating elements: N and H. A nitrogen atom can form bonds with all three neighbors of the vacancy defect. A hydrogen atom on the other hand can saturate only the atom located at the *f*-site. In both situations, we place the add-atom near the unsaturated atom and perform DFT simulations to obtain a “repaired” defect structure. The hydrogen atom partially saturates the defective site, while the nitrogen atom completely annihilates the defective state as evident from the electron density map and the DOS plots shown in Fig. 3.

The electron density map indicates the H atom to retain the C_2 symmetry of the defect structure. The N-passivated defect structure on the other hand annihilates the five to nine structures completely and brings back the C_3 symmetry of the sp^2 lattice. The sharpest peak is seen at the *f*-site. Passivation, however, annihilates the defect state completely.

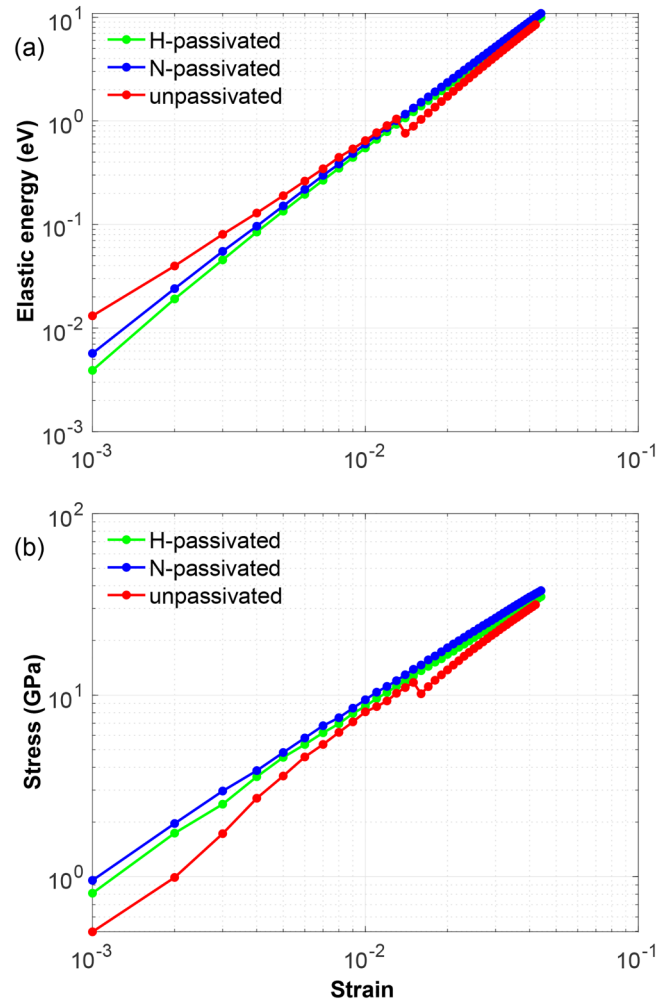


FIG. 4. (a) Elastic energy as a function of applied strain in a log-log scale. The drop in energy density is caused by the JTRR at around 0.017 strain. The energy difference at the discontinuity is 0.30 eV, which is released due to JTRR. (b) Stress as a function of strain in a log-log scale. The stress-reduction due to JTRR is around 0.2 GPa.

B. Deformation response of monovacancy

1. Structural reconstruction

We investigated the deformation response of four lattices with different chiralities to understand the electron redistribution at the monovacancy. The elastic energy and stress response of the unpassivated lattice are shown in Fig. 4. The curve is presented in a log-log plot to better reveal the stress-strain response of the lattice at the early stages of linear mechanical deformation. To assess the role of passivation, results of the unpassivated lattice are compared with the H-passivated and N-passivated cases.

Fitting a second-order curve of the form $\sigma = C_1\epsilon + C_2\epsilon^2$ to the stress-strain data, we obtain $C_0 = 943.4$ GPa and

$C_2 = -1926.0$ GPa, which are Young's modulus and the second-order elastic modulus, respectively. From the logarithmic plot, we expect the data to satisfy the following relation:

$$\ln \sigma = \ln C_1 \epsilon + 2 \ln C_2 \epsilon = \ln (C_1 C_2) + 3 \ln \epsilon.$$

The defect-free, N-passivated, and H-passivated lattices show such a linear relationship. A small drop in the elastic energy and stress is evident for the unpassivated case, where the elastic energy of the deformed lattice is computed relative to the undeformed state as $E_{\text{elastic}} = E(\epsilon) - E(0)$. The drop is associated with a reorientation of the defect structure, as illustrated in Fig. 5. The reorientation event comprises breaking of the nearest-neighbor bond [qr in Fig. 5(c)] and formation of a new nearest-neighbor bond [pq in Fig. 5(d)]. We call this *Jahn-Teller re-reconstruction* (JTRR). It is a second-order reconstruction as it takes place under a symmetry-breaking deformed condition and is mechanically reversible. In the undeformed condition, the defect structure has a C_3 symmetry. There are three possible degenerate configurations separated by an energy barrier of around 0.1 eV.¹³ Symmetry-breaking deformation lifts the degeneracy and stabilizes the orientation of the defect relative to the loading direction. It increases the energy barrier for the transition of the strained defect structure into the other two possible orientations.

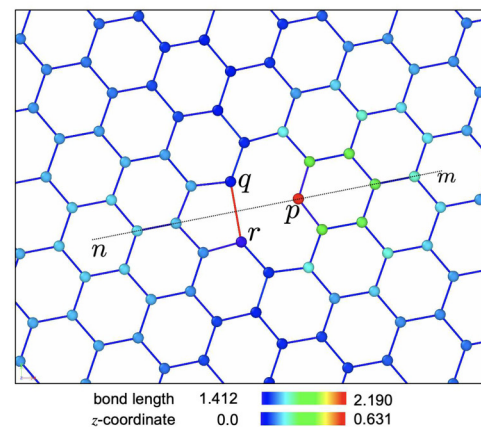
The change in the elastic energy in JTRR is around 0.3 eV. It occurs between 1.6% and 1.7% macroscopic strain. It accounts for the energy barrier that the atoms at the defect core must overcome for the reorientation event to take place. JTRR is a stable but reversible process, as it occurs in the linear regime of mechanical deformation. As such, removal of loading would take the defect orientation back to its initial orientation state. In the undeformed condition, the degenerate structures have equal probability to appear at a defective site. The energy barrier for transition between these structures is reported to lie between 0.1 and 0.76 eV,^{13,37–39} which is smaller than the defect formation energy of 7.0 eV in graphene¹³ and the migration energy of 1.7 eV.¹³ At 300 K, the cycle frequency for the dynamic reconstruction can be calculated from Eq. (3),

$$\kappa = \kappa_0 \exp \left(-\frac{E_a}{k_B T} \right), \quad (3)$$

where $\kappa_0 = 10^{13}$ Hz is the Debye frequency, k_B is the Boltzmann constant, T is the temperature, and E_a is the activation energy that ranges from 2.0×10^{11} to 1.80 Hz.

The strain energy per atom can be calculated by fitting a quadratic equation to the DFT-generated energy/atom and strain data. It gives $E_{\text{atom}} = 22.43\epsilon^2$, where E_{atom} is the elastic energy per atom. For 5%, 10%, and 20% bond strain, $E_{\text{atom}} = 0.056$, 0.2243, and 0.8972 eV/atom, respectively. How this strain affects the activation energy barrier depends on the orientation of the JT bond. For situations wherein the JT bond has a higher direction cosine relative to the loading direction [as shown in Fig. 5(c)], any nonzero applied strain will lower the energy barrier and facilitate the breaking of bond qr and formation of bond pq , whereas if the JT bond has small direction cosine relative to the loading direction [as

(a) before JTRR



(b) after JTRR

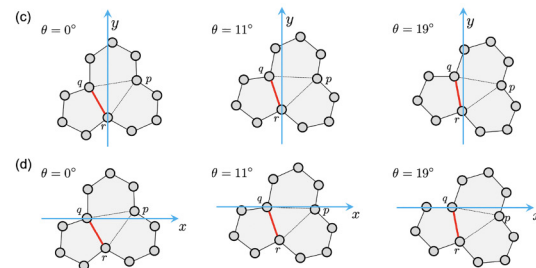
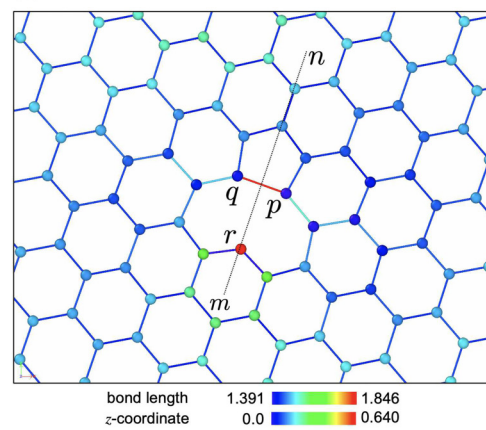


FIG. 5. Reconstruction at the defect core for a high-symmetry lattice of chirality 0° (a) before JTRR at $\epsilon = 0.016$ and (b) after JTRR at $\epsilon = 0.017$. Bond length and atomic positions shown by the colors are in the units of Å. The line mn represents the line of defect symmetry. Reconstruction at the defect core for a low-symmetry lattice of chirality 19° before JTRR at $\epsilon = 0.016$ and after JTRR at $\epsilon = 0.017$. Pentagon-nonagon structures for three different chiral angles for loading along (c) the y -direction and (d) the x -direction. The direction cosines of the bonds pq are the minimum when loading is applied along the y -direction, while they are the maximum when loading is applied along the x -direction. For loading along the y direction, the qr bond breaks beyond a critical strain and it leads a pathway for the pq bond to reconstruct, facilitated by Poisson's contraction, whereas for loading along the x direction, the qr bond remains as the JT bond and loading stabilizes its orientation (prohibiting any reconstruction of the pq or pr bond).

shown in Fig. 5(d)], applied strain will increase the energy barrier for breaking the qr bond as it will subject to compression.

Symmetry-breaking strain reduces the symmetry of the defect structure and lifts the degeneracy. It stabilizes the defect structure in two ways. First, if the direction cosine of the JT bond relative to the loading direction is the highest among the three probable bonds (pr , qr , and pr in Fig. 4), it experiences the largest stretching and hence breaks beyond a critical strain (of around 1.7% for $\theta = 19^\circ$). Second, if the direction cosine is the smallest, the bond experiences less force and Poisson's effect contracts the bond further, eliminating the possibility of any second-order JTR. As shown in Fig. 5(c-d), a monovacancy in a lattice with chirality 0° , 11° , and 19° undergoes JTRR for loading along the y -direction, whereas for loading along the x -direction, the JT bonds remain as are. In either case, finite strain stabilizes the defect orientation by increasing the energetic barrier needed to break the JT bond. The higher the strain, the more stable the reconstructed defect structure. As the JT bond is perpendicular or close to perpendicular to the loading direction (after JTRR or for orientations with the JT bonds having the lowest direction cosines), accessibility to other two possible reconstructed structures would depend on the increase in length of the bond of the highest direction cosine. The barrier for forming bonds of this bond will increase as $22.43\epsilon^2$. This points to an important conclusion that symmetry-breaking strain can play a significant role in aligning and stabilizing the defect structure relative to the loading direction.

2. Electron redistribution

To develop a quantitative understanding of reorientation, we investigate the total electron occupation over the valence orbitals before and after JTRR. Under applied deformation, the “change in the electron redistribution” provides a unique measure of the role of deformation in modulating the electronic characteristic of the individual orbitals of the atoms at and nearby the defective site. The total number of electrons in the system is a constant, regardless of the deformation state or defect orientation. The first derivative of the total charge, as given in Eq. (4), with respect to strain provides a quantitative measure of the strain induced alteration in electron occupation in the individual orbitals,

$$\frac{d\chi}{d\epsilon} = \frac{\sum_{i=1}^N d(\chi_i^s + \chi_i^{p_x} + \chi_i^{p_y} + \chi_i^{p_z})}{d\epsilon} = 0. \quad (4)$$

In a defective system, the spatial effects of the strain fields emanating from the defect site are inhomogeneous but finite as long as the defect is not interacting with another defect. In such a situation, assuming the localized charge redistribution to be confined within a region Ω around the defect, we can write

$$\frac{d}{d\epsilon} \left(\int_{\Omega} \chi(r) dr \right) = 0, \quad (5)$$

where $\chi(r)$ is the total charge at location r . This equation states that the strain induced variation in the total electron occupation around the defective site is zero within Ω . Redistribution is, therefore,

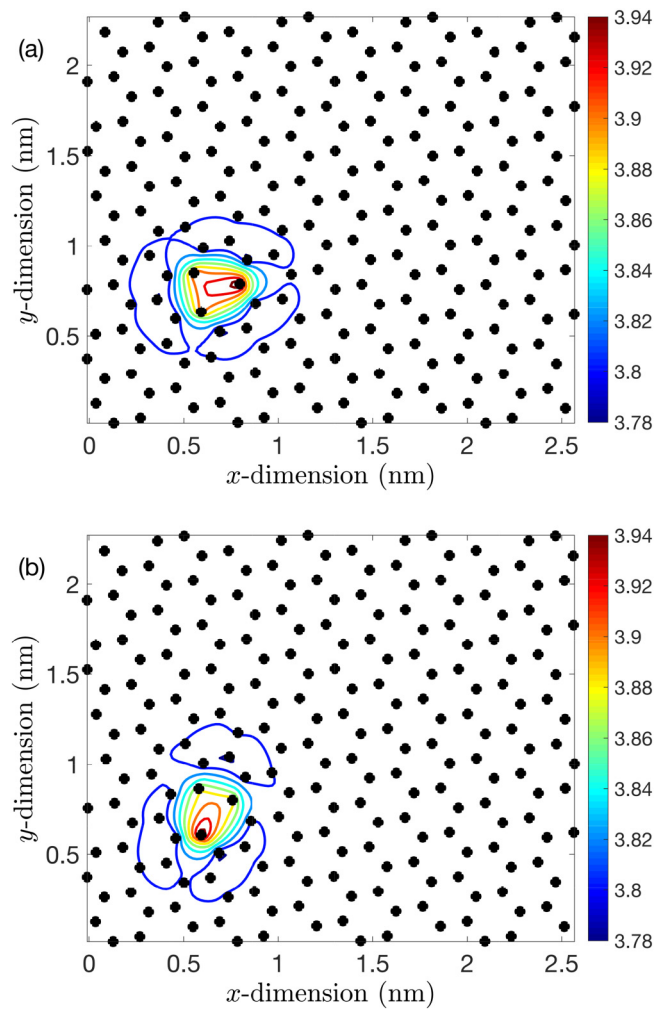


FIG. 6. Contour plot of the charge occupation map constructed by integrating the charges over the s , p_x , p_y , and p_z orbitals (a) before and (b) after Jahn-Teller reconstruction. The small spatial coverage of the charge occupations at the defective site highlights the localized character of both the JTR and JTRR. The maximum, minimum, and average occupations are 3.96, 3.77, and 3.80, respectively, before and after JTRR. The transition takes place at around 0.017 macroscopic strain state.

confined within a smaller regime surrounding the defect. Outside Ω , electron redistribution is uniform and follows the bulk behavior.

A continuum scale representation of the electronic charge surrounding the defect core before and after JTRR shows similar distribution patterns (both qualitatively and quantitatively), as displayed in Fig. 6. The maximum occupation remains at the defective site comprising the a , b , and f sites. These sites are surrounded by atoms with a depletion in their electron occupation (as shown by the blue contours). The strain induced reorientation causes no substantial modulation to the charge distribution pattern or to the net electron occupation. The individual orbitals, however, show a

consistent spatial alteration in their electron occupation. The changes in electron occupations in the individual orbitals $\Delta\chi_s$, $\Delta\chi_{p_x}$, $\Delta\chi_{p_y}$, and $\Delta\chi_{p_z}$ before and after the reorientation at the *f*-site are -6.122% , -0.6066% , 1.47% , and 1.54% , respectively, where $\Delta\chi_i = \chi_i^{\text{after}} - \chi_i^{\text{before}}$ and $i \in \{s, p_x, p_y, p_z\}$. The net change around the defect satisfies the condition that

$$\sum (\Delta\chi_s + \Delta\chi_{p_x} + \Delta\chi_{p_y} + \Delta\chi_{p_z}) = 0,$$

where the sum runs over all the affected atoms by the defect core. The characteristic behavior of JTTR is, thus, well-captured by the extremum of occupations in different orbitals. The maximum electron occupation over all atomic sites at different strain states for each of the orbitals shows a clear indication of the JTTR event. This is shown in Fig. 7.

Before the JTTR, the maximum occupation in the *s*, *p*_x, and *p*_z orbitals increases with increasing strain (applied along the

y-direction), while it decreases in the *p*_y orbital. The increase in occupation in *p*_x and *p*_z orbitals is much more rapid compared to the decrease in the occupation in the *p*_y orbital. Also, the rate of increase in occupation is higher for loading along 0° . After JTTR (appearing around $\epsilon = 0.017$), the maximum electron occupation decreases in the *s* orbital but continues to increase in the *p*_z orbital and the trend is independent of the chirality of the lattice. For the *p*_x orbital, the maximum occupation is chirality-dependent. For 0° and 11° chiralities, the maximum occupation in the *p*_x orbital reaches a constant value beyond JTTR, while, for the 19° and 30° chiralities, the maximum occupation decreases with increasing strain. The change in electron occupation manifests an anisotropic pattern. Furthermore, the maximum electron occupation at the defective site changes dramatically after the JTTR. Tension decreases the electron occupation in an orbital, while contraction increases the occupation.

We also performed calculations to find the partial density of states (PDOS) at two representative sites at the defect core and one

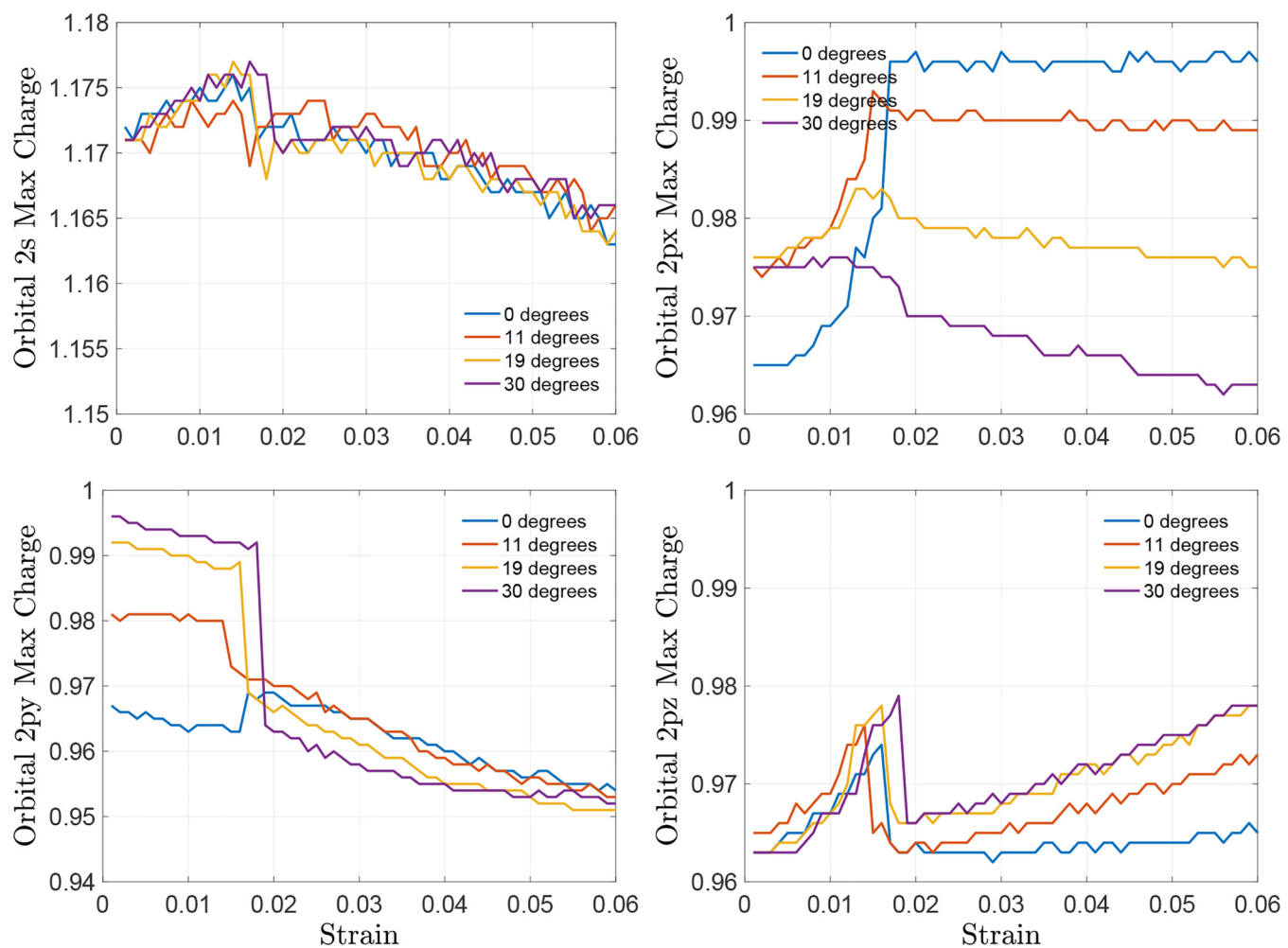


FIG. 7. Maximum electron occupation in the *s*, *p*_x, *p*_y, and *p*_z orbitals as a function of applied macroscopic strain. For each orbital type, the JTTR occurs at around 0.017.

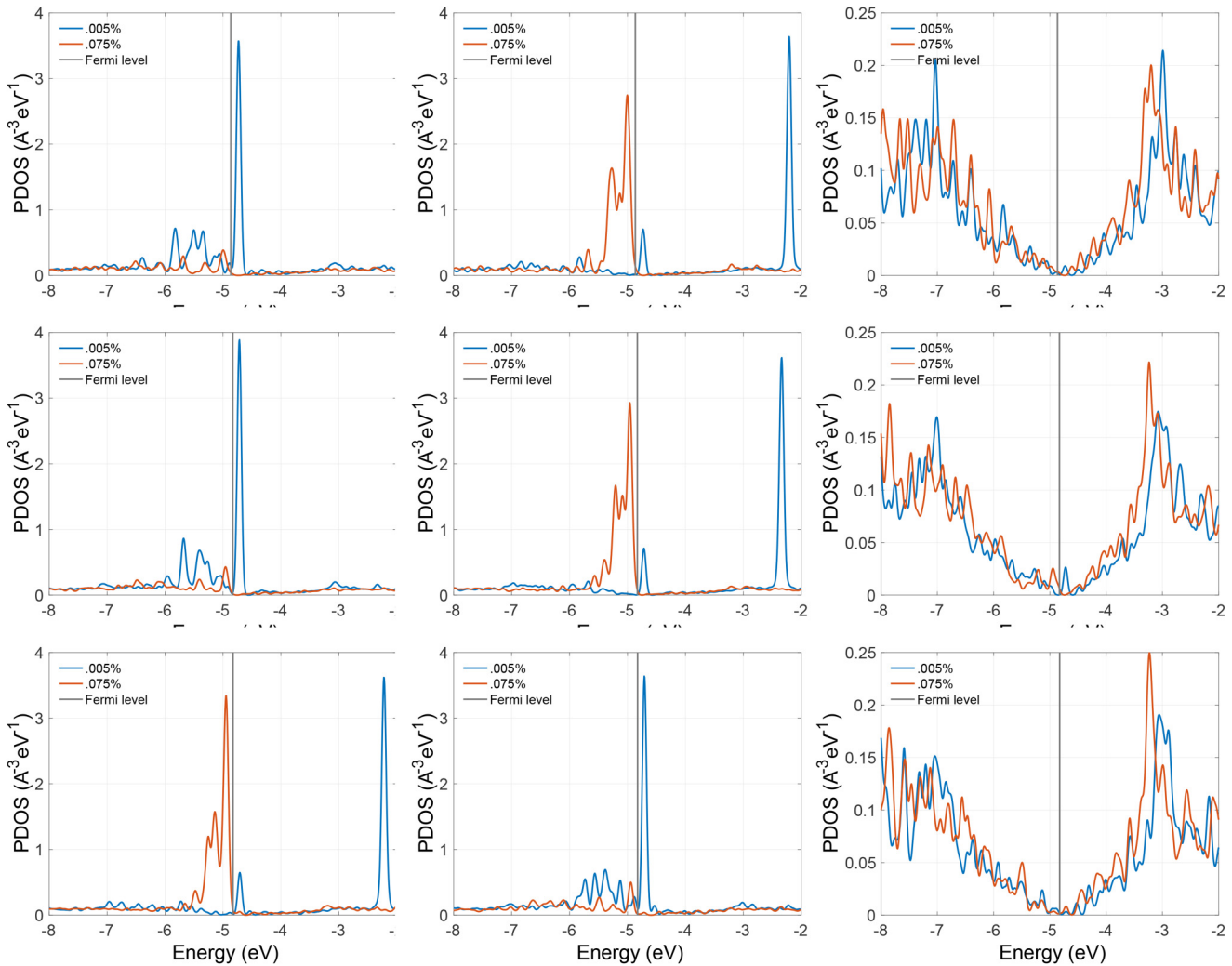


FIG. 8. (First row) $\theta = 0^\circ$, (second row) $\theta = 11^\circ$, and (third row) $\theta = 19^\circ$. These figures show the partial density of states of the defective lattice at their respective orientation angles with two different levels of deformation applied (0.005% and 0.075%). The first column of figures represents the partial density of states for the particle closest to the center of the mono vacancy, the second column depicts the partial density of states for the particles second closest to the center of the monovacancy, and the third column depicts the partial density of states for a bulk particle. The vertical lines in each graph denote the Fermi energy in the undeformed lattice for each of the chiralities considered in this work.

site at the bulk. Comparing a bulk atom to an atom surrounding the monovacancy, we see that the atoms surrounding the vacancy have a series of large peaks around the Fermi level of the undeformed graphene, as illustrated in Fig. 8. The PDOS figure for the bulk atom (the third column) is very similar to the total DOS of the lattice. However, the atoms close to the center of the monovacancy exhibit a higher density of states around the Fermi level energy. The closer the atom is to the center of the defect, the more pronounced this effect is. Also, the carbon atoms bordering the monovacancy that are farther away from the center of the defect exhibit PDOS that is more similar to the DOS or the bulk PDOS.

The reactivity of the lattice is, therefore, entirely controlled by the defective site, and the deformation induced JTTR changes the site-dependent activity by modulating the sites for the maximum PDOS.

3. Magnetic moment modulation

To investigate the effect of spin-polarization, we considered the 19° chiral lattice case and compared the results obtained with and without the spin-polarization effects. Results do not show any significant effect of spin-polarization for any of the mechanical

states discussed in the paper. Also, the total electronic charge, which is a conserved quantity, remains unaffected by spin-polarization. As such, at a given atomic site r , the total charge, which is a sum over the charges in the bond-forming electronic orbitals, satisfies the simple condition that $n(r) = n_{sp}(r)$, where n_{sp} is the electron density when the spin-polarization effects are included in the calculation. However, spin-polarization affects the decomposition of the spin-up and spin-down electronic charges. In terms of the spin-up and spin-down densities, the total density in these two calculations can be written as

$$n(r) = n^+ + n^-, \quad (6)$$

$$n_{sp}(r) = n_{sp}^+ + n_{sp}^-. \quad (7)$$

Far from the defect, $n^+ = n_{sp}^+$ and $n^- = n_{sp}^-$, suggesting no effect of spin-polarization on the decomposition of the spin-up and spin-down occupations. On the other hand, for the atoms at the defective site, the electron density satisfies the following inequalities:

$$n^+ \neq n_{sp}^+, n^- \neq n_{sp}^-. \quad (8)$$

As a result, the magnetic moment or magnetization density, denoted here as $m(r)$ and calculated as the difference between the spin-up and spin-down charges, becomes nonzero at the defective site,

$$m(r) = n_{sp}^+ - n_{sp}^- \neq 0. \quad (9)$$

The total moment of the system before JTTR is $-1.3620\mu_B$, and it changes to $1.2280\mu_B$ after the JTTR. As the moment can take either positive or negative signs arbitrarily, we consider the absolute values of the magnetic moment to evaluate the effect of JTTR on magnetization. From that perspective, both values fall within the reported range of $1.12\mu_B$ – $1.53\mu_B$.⁵ The contributions of the individual orbitals can be obtained by decomposing the total spin-up and spin-down charges as a sum over the respective charges in the individual orbitals. Mathematically, this can be expressed as

$$m(r) = \sum_{i \in \{s, p_x, p_y, p_z\}} (n_i^+ - n_i^-) \quad (10)$$

$$= (n_s^+ - n_s^-) + (n_{p_x}^+ - n_{p_x}^-) + (n_{p_y}^+ - n_{p_y}^-) + (n_{p_z}^+ - n_{p_z}^-) \quad (11)$$

$$= m_s(r) + m_{p_x}(r) + m_{p_y}(r) + m_{p_z}(r). \quad (12)$$

The orbital-dependent magnetic moments, $m_i(r)$, where $i \in \{s, p_x, p_y, p_z\}$ is shown in Fig. 9. Before JTTR, the net magnetic moment is negative and, after JTTR, it is positive. This switching of the net magnetic moment results from a similar change in the s , p_x , p_y , and p_z orbitals, and the overall behavior is dominated by the change in the occupations in the p_y orbitals. This dominance is a direct consequence of the loading applied along the y -direction that causes the bonds to stretch along the y -direction and Poisson's contraction of the electronic orbitals along the x - and z -directions.

4. Electronic structural basis of JTTR

To investigate the atomistic basis of the transition angle, we first explore the maximum bond length in the lattice. The JT bond is consistently the longest bond in the lattice, regardless of the strain state. The maximum bond length at any given strain state is calculated from the expression that $r_{\max}(\epsilon) = \max r_{ij}(\epsilon) = \max |(\mathbf{x}_i - \mathbf{x}_j)|$. Plotting this quantity, we find r_{\max} to increase with increasing strain. It reaches a maximum at around 0.017 strain state and drops to a lower value following the JTTR event, as depicted in Fig. 10. For all tested orientation angles, the reconstruction of bonds begins at approximately 1.88 Å, which is 32.39% higher than the equilibrium bond length of 1.42 Å. Prior to undergoing a reattachment, the bond length increases up to a peak value of 2.12 Å for loading along 0° chiral angle of the lattice. The peak point depends on the chirality of the lattice due to the associated change in the direction cosine of the bond relative to the loading direction. At the peak point, the reconstruction bond detaches from one atom, swings upward, and reattaches itself to another atom at the defect site. This event results in a sudden drop in the length of the reconstruction bond as the JT bond aligns itself normal to the loading direction. The bond length decreases gradually with further deformation before beginning material failure. The strain state for causing the maximum bond length transition can be taken as a critical feature of bond deformation in the lattice and related with the maximum bond force.

As the total energy of the system has a number of components, the origin of the bond rupture force can be traced by evaluating the change in the total energy and its constituents with respect to the applied strain. The total electronic energy of the lattice, E_{total} , is a sum over the kinetic energy of the electrons, the Hartree energy, the exchange-correlation energy, the ion-electron interaction energy, and the ion-ion interaction energy. The strain-dependent decomposition is, thus,

$$E_{\text{total}} = E_{\text{kinetic}} + E_{\text{Hartree}} + E_{\text{xc}} + E_{\text{ie}} + E_{\text{ii}}.$$

Each of the energy-quantities depends on the interatomic separation distance, hence is strain-dependent. The resultant interatomic force arising from an increased separation distance originates from different parts of the total energy. The first derivative of the energy terms yields a direct measure of the interatomic bond force arising from different electronic interactions in the lattice. The total force can be written as

$$\begin{aligned} F_{\text{total}} &= \frac{\partial E_{\text{total}}}{\partial r} \\ &= \frac{\partial E_{\text{kinetic}}}{\partial r} + \frac{\partial E_{\text{Hartree}}}{\partial r} + \frac{\partial E_{\text{xc}}}{\partial r} + \frac{\partial E_{\text{ie}}}{\partial r} + \frac{\partial E_{\text{ii}}}{\partial r} \\ &= F_{\text{kinetic}} + F_{\text{Hartree}} + F_{\text{xc}} + F_{\text{ie}} + F_{\text{ii}}. \end{aligned}$$

To determine the effects of the individual components of the energy to the interatomic force, we normalize the energies using the following general form:

$$\bar{\chi} = \frac{\chi - \chi_\infty}{\max(|\chi - \chi_\infty|)}, \quad (13)$$

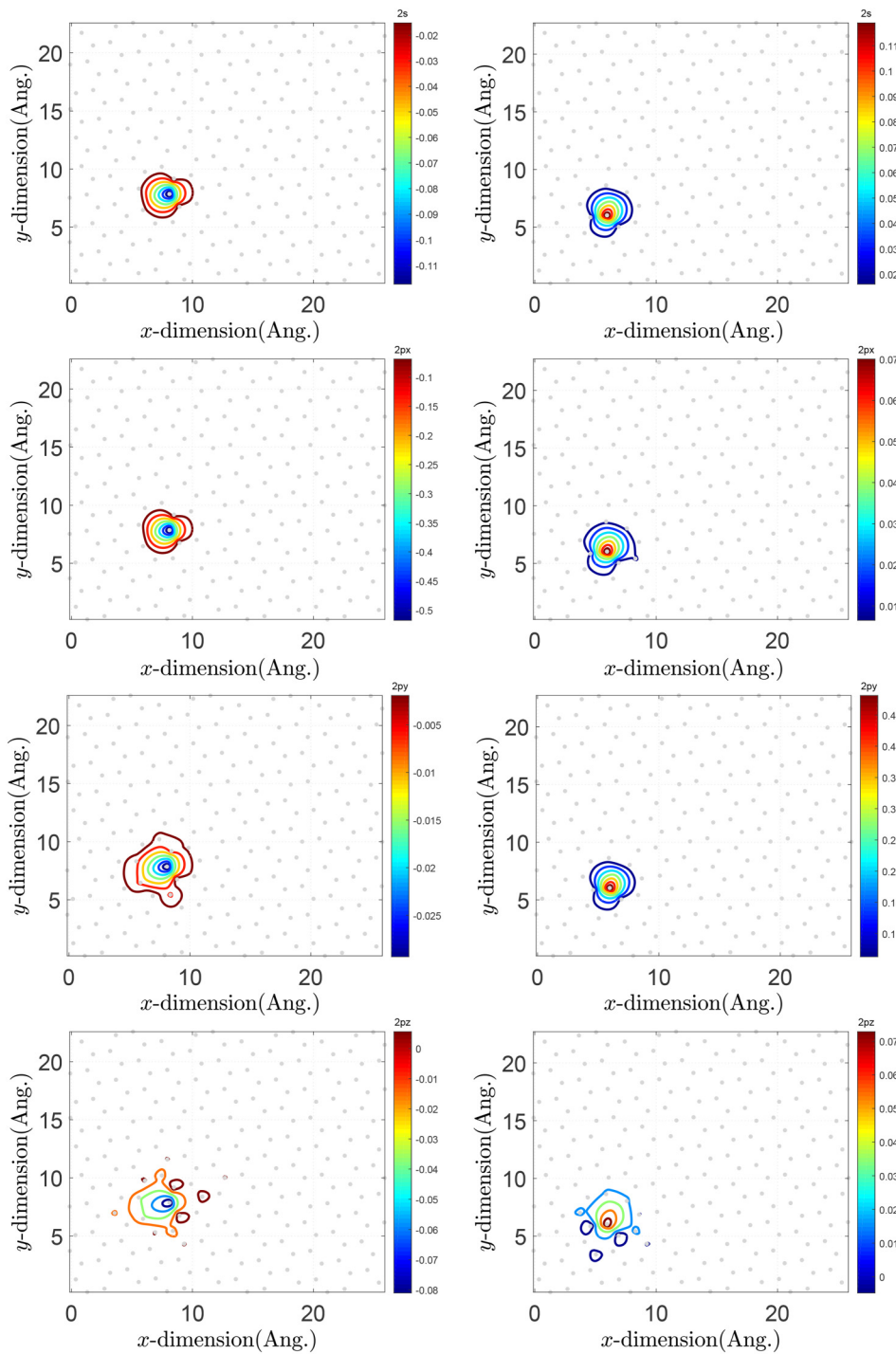


FIG. 9. Contour plot of the magnetic moment (left column) before JTTR and (right column) after JTTR in (first row) s-orbital, (second row) p_x -orbital, (third row) p_y -orbital, and (fourth row) p_z -orbital. The ash-colored filled circles represent atomic positions.

where $\bar{\chi}$ is the normalized energy, $\chi \in \{E_{\text{kinetic}}, E_{\text{Hartree}}, E_{\text{XC}}, E_{\text{ie}}, E_{\text{ii}}\}$, and χ_∞ is the energy of interatomic interaction at long distance. The respective force components are then calculated from first-order differentiation using the central difference formula. To

examine the behavior of the total energy and force as well as different components of the total energy, we performed DFT simulations under the symmetry-preserving hydrostatic deformation in which the lattice parameters are scaled uniformly in all directions and the

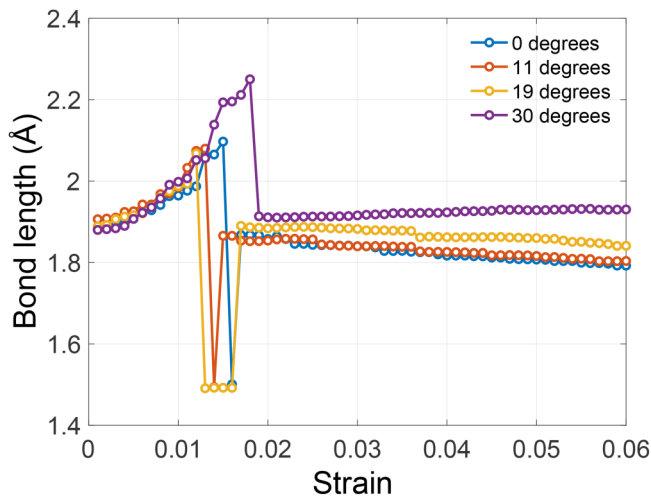


FIG. 10. The length of the reconstruction bond (the max bond length in the lattice) as a function of applied macroscopic strain for four chiral angles of the lattice. The drop in the bond length indicates the appearance of the second-order JT reconstruction. They appear around 1.5%–1.8% macroscopic strain states. While before JTTR the maximum bond length is at an angle higher than 45° relative to the loading direction, after reconstruction the maximum bond length appears at 90° to the loading direction. As a result, the JT bond experiences higher Poisson's contraction, and its length starts going down for most of the chiral angles.

energy and force are computed at each of the deformation states. As plotted in Fig. 11, the interatomic interaction is zero at separation distance larger than 3 Å. The total bond force is the maximum at $\epsilon = 0.245$ and it is equal to $(1 + 0.245)r_0 = 1.7679$ Å, where $r_0 = 1.42$ Å is the equilibrium bond length. The initial JT bond length is higher than this length. This prompts the question as to what type of electronic interaction forms the physical basis for the JT bond. As noted before, the JTTR occurs at a macroscopic applied strain state of $\epsilon_{\text{bond}} = 1.434$, which is equal to 3.456 28 Å and much higher than r_0 . The individual energy and force curves for different combinations of ion and electron interactions are plotted in Fig. 11. The XC and ion-electron energies are purely attractive, the ion-ion energy is purely repulsive, and the kinetic energy has a minimum at $r_{ok} = 0.9057$ bond strain. The bond force due to the kinetic energy of the electrons is the maximum at 1.434 Å. The maximum nearest-neighbor bond length in the defective lattice under uniaxial macroscopic strain of $\epsilon = 0.016$ is 2.12 Å, which is close to the value of a bond length of $1.42 \times 1.434 = 2.03$ Å. The onset of the JTTR can be attributed to the variation of the kinetic energy of the electrons. As soon as the bond stiffness due to the kinetic energy variation with respect to strain becomes negative, the JT bond ruptures and undergoes a reorientation, triggering the JTTR event. The JTTR is mediated by Poisson's contraction that facilitates the atoms forming the bond (with the minimum direction cosine to the loading direction) at the defective sites to interact stronger and come closer. This event

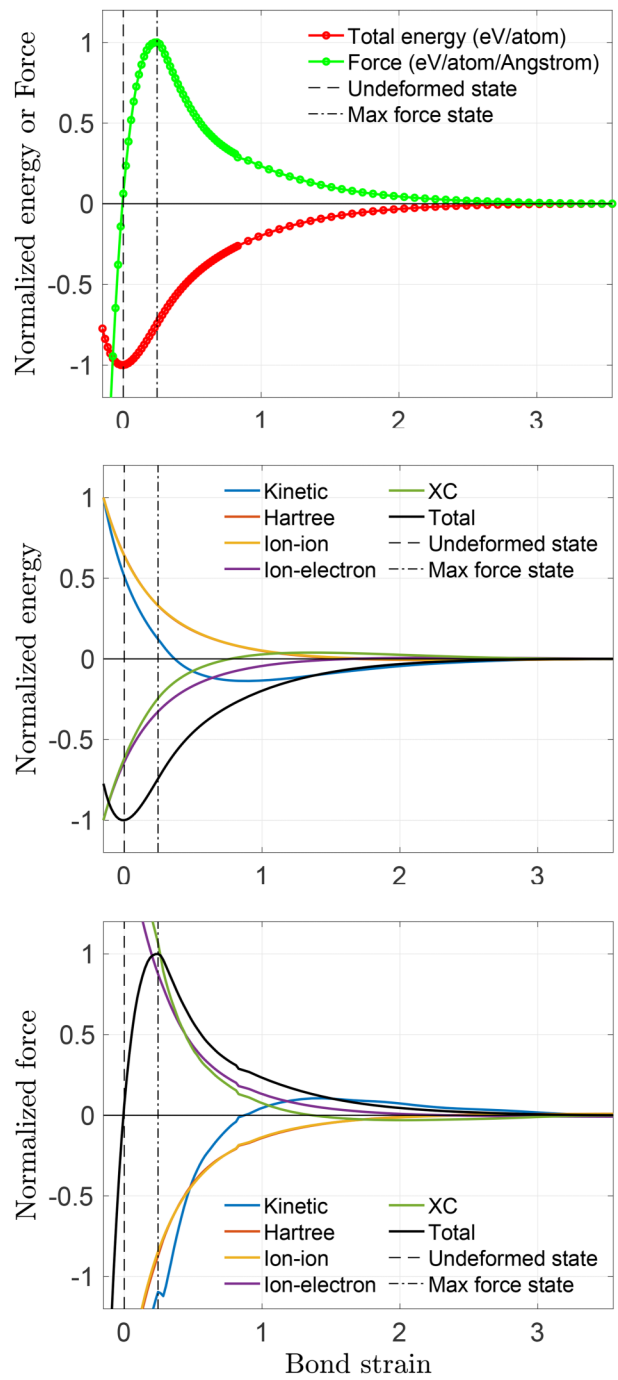


FIG. 11. (Top) Normalized interatomic total force/energy vs strain. (Middle) Normalized interaction energy components vs strain. (Bottom) Normalized interaction force components. Marked in the dashed vertical lines is the strain at which the bond is under equilibrium. Marked in the centerline is the strain at which the total bond force is the maximum. The maximum total bond force occurs at $\epsilon = 0.245$ Å. The maximum bond force due to the kinetic energy of the electrons occurs as $\epsilon = 143.39\%$.

is, thus, dependent on the chirality of the lattice: the higher the chirality, the higher the direction cosine and the higher the strain state for triggering the JTTR event.

IV. CONCLUSIONS

To summarize, we report a first-principle observation of change in the orientation of a pentagon–nonagon monovacancy structure in graphene under symmetry-breaking loading. The reorientation occurs at around 1.7% applied strain, and this number has a close relationship with the maximum bond force. It arises from the change in the kinetic energy of electrons as a function of the bond length. The kinetic energy of the electrons provides an interesting reversible defect structure. Also, since the JTTR occurs in the linear regime of mechanical deformation, release of applied strain gives the initial JTR structure orientation back.

As a consequence of the bond reconstruction event, the pattern of electron distribution undergoes a commensurate reconstruction process. It changes the electronic character of the atoms at the defect site. Furthermore, the electron distribution at the defective site is strongly inhomogeneous in each of the electronic orbitals that form the sp^2 bonds in the lattice. The elastic field as well as the electronic consequence of the charge inhomogeneity are highly localized and their effects are inconsequential beyond around 5 Å distance from the defect core. The inhomogeneity is confined within a smaller spatial regime surrounding the defect site such that the alteration of electronic occupation is confined within a small distance surrounding the defect. Moreover, applying the Mulliken population analysis scheme, we find that the electron distribution pattern is dominated by the p_x and p_z orbitals, which are aligned along the lateral and out-of-plane directions, respectively. The chirality of the lattice has a weak influence on the reconstruction of the electron population among the orbitals. The JTTR process changes the magnitude of the magnetic moment from $1.36\ \mu_B$ to $1.22\ \mu_B$ at the defect site.

The observations suggest that a change in the direction of the symmetry-breaking deformation (beyond a critical strain) can produce reversible magnetic effects. Therefore, for a random distribution of defects in graphene, application of uniaxial loading along the y -direction would stabilize and align all the defect's orientations toward the y -direction. A subsequent uniaxial loading along the x -direction can then change all the orientations by 120° . Alternating uniaxial strain between the x and y directions can, thus, offer a viable route for achieving controllable magnetic effects. Additionally, the JTTR event in selected sites can be controlled by passivation of unsaturated atoms: depending on the number of valence electrons of the passivating atom, the defect structure either saturates partially or completely. In an array of MV defects, one could obtain a number of interesting magnetic effects by controlling the defect density, controlling their reactivity through passivation, and modulating their electronic structure by applying a combination of orthogonal uniaxial strains.

AUTHORS' CONTRIBUTIONS

C. A. and T. H. contributed equally to this work.

ACKNOWLEDGMENTS

The authors are grateful to the reviewers for providing a number of insightful comments that led to a substantial improvement in the discussions. C. Andreasen acknowledges UD's K-12 program, and J. Hatoum acknowledges the Delaware Energy Institute's Summer Scholar program. The authors also acknowledge Heran Yang's help in proofreading the manuscript.

DATA AVAILABILITY

The data that support the findings of this study are available from the corresponding author upon reasonable request.

REFERENCES

- ¹A. Avsar, H. Ochoa, F. Guinea, B. Özyilmaz, B. Van Wees, and I. J. Vera-Marun, *Rev. Mod. Phys.* **92**, 021003 (2020).
- ²G.-D. Lee, C. Wang, E. Yoon, N.-M. Hwang, D.-Y. Kim, and K. Ho, *Phys. Rev. Lett.* **95**, 205501 (2005).
- ³K. S. Novoselov, A. K. Geim, S. V. Morozov, D. Jiang, Y. Zhang, S. V. Dubonos, I. V. Grigorieva, and A. A. Firsov, *Science* **306**, 666 (2004).
- ⁴V. O. Özçelik, H. H. Gurel, and S. Ciraci, *Phys. Rev. B* **88**, 045440 (2013).
- ⁵O. V. Yazyev and L. Helm, *Phys. Rev. B* **75**, 125408 (2007).
- ⁶M. Pizzochero, K. Čerňevič, G. B. Barin, S. Wang, P. Ruffieux, R. Fasel, and O. V. Yazyev, "Quantum electronic transport across 'bite' defects in graphene nanoribbons," *2D Mater.* **8**, 035025 (2021).
- ⁷R. R. Nair, I.-L. Tsai, M. Sepioni, O. Lehtinen, J. Keinonen, A. V. Krasheninnikov, A. H. Castro Neto, M. I. Katsnelson, A. K. Geim, and I. V. Grigorieva, "Dual origin of defect magnetism in graphene and its reversible switching by molecular doping," *Nat. Commun.* **4**, 1–6 (2013).
- ⁸O. V. Yazyev, *Phys. Rev. Lett.* **101**, 037203 (2008).
- ⁹M. Casartelli, S. Casolo, G. Tantardini, and R. Martinazzo, *Phys. Rev. B* **88**, 195424 (2013).
- ¹⁰A. Castellanos-Gómez, M. Wojtaszek, R. Smit, N. Tombros, N. Agrait, B. Van Wees, G. Rubio-Bollinger *et al.*, *arXiv:1210.4147* (2012).
- ¹¹P. Lehtinen, A. Foster, and Y. Ma, *Phys. Rev. Lett.* **93**, 187202 (2004).
- ¹²B. Wang and S. T. Pantelides, *Phys. Rev. B* **86**, 165438 (2012).
- ¹³A. El-Barbary, R. Telling, C. Ewels, M. Heggie, and P. Briddon, *Phys. Rev. B* **68**, 144107 (2003).
- ¹⁴T. Hao, T. Ahmed, R. J. Mou, J. Xu, S. Brown, and Z. M. Hossain, *J. Appl. Phys.* **127**, 204301 (2020).
- ¹⁵R. Nair, M. Sepioni, I.-L. Tsai, O. Lehtinen, J. Keinonen, A. Krasheninnikov, T. Thomson, A. Geim, and I. Grigorieva, *Nat. Phys.* **8**, 199 (2012).
- ¹⁶T. G. Pedersen, C. Flindt, J. Pedersen, N. A. Mortensen, A.-P. Jauho, and K. Pedersen, *Phys. Rev. Lett.* **100**, 136804 (2008).
- ¹⁷L. D. Carr and M. T. Lusk, *Nat. Nanotechnol.* **5**, 316 (2010).
- ¹⁸W. Han, R. K. Kawakami, M. Gmitra, and J. Fabian, *Nat. Nanotechnol.* **9**, 794 (2014).
- ¹⁹H. Zhang, G. Lee, and K. Cho, *Phys. Rev. B* **84**, 115460 (2011).
- ²⁰J.-U. Lee, D. Yoon, and H. Cheong, *Nano Lett.* **12**, 4444 (2012).
- ²¹F. Liu, P. Ming, and J. Li, *Phys. Rev. B* **76**, 064120 (2007).
- ²²H. Zhao and N. Aluru, *J. Appl. Phys.* **108**, 064321 (2010).
- ²³H. Zhao, K. Min, and N. Aluru, *Nano Lett.* **9**, 3012 (2009).
- ²⁴I. Frank, D. M. Tanenbaum, A. M. van der Zande, and P. L. McEuen, *J. Vac. Sci. Technol. B* **25**, 2558 (2007).
- ²⁵C. Lee, X. Wei, J. W. Kysar, and J. Hone, *Science* **321**, 385 (2008).
- ²⁶K. Min and N. R. Aluru, *Appl. Phys. Lett.* **98**, 013113 (2011).
- ²⁷Z. Li, I. A. Kinloch, R. J. Young, K. S. Novoselov, G. Anagnostopoulos, J. Parthenios, C. Galiotis, K. Papagelis, C.-Y. Lu, and L. Britnell, *ACS Nano* **9**, 3917 (2015).
- ²⁸A. V. Krasheninnikov and R. Nieminen, *Theor. Chem. Acc.* **129**, 625 (2011).

- ²⁹T. Trevethan, C. D. Latham, M. I. Heggie, P. R. Briddon, and M. J. Rayson, *Nanoscale* **6**, 2978 (2014).
- ³⁰J. Kotakoski, A. Krasheninnikov, and K. Nordlund, *Phys. Rev. B* **74**, 245420 (2006).
- ³¹R. Dettori, E. Cadelano, and L. Colombo, *J. Phys. Condens. Matter* **24**, 104020 (2012).
- ³²J. T. Robinson, M. K. Zalalutdinov, C. D. Cress, J. C. Culbertson, A. L. Friedman, A. Merrill, and B. J. Landi, *ACS Nano* **11**, 4745 (2017).
- ³³A. W. Robertson, B. Montanari, K. He, C. S. Allen, Y. A. Wu, N. M. Harrison, A. I. Kirkland, and J. H. Warner, *ACS Nano* **7**, 4495 (2013).
- ³⁴A. M. Valencia and M. J. Caldas, *Phys. Rev. B* **96**, 125431 (2017).
- ³⁵M. Sturge, in *Solid State Physics* (Elsevier, 1968), Vol. 20, pp. 91–211.
- ³⁶H. C. Longuet-Higgins, U. Öpik, M. H. L. Pryce, and R. Sack, “Studies of the Jahn-Teller effect. II The dynamical problem,” *Proc. R. Soc. Lond. A Math. Phys. Sci.* **244**, 1–16 (1958).
- ³⁷Z. Hou and K. Terakura, *J. Phys. Chem. C* **119**, 4922 (2015).
- ³⁸J. D. Wadey, A. Markevich, A. Robertson, J. Warner, A. Kirkland, and E. Besley, *Chem. Phys. Lett.* **648**, 161 (2016).
- ³⁹R. Babar and M. Kabir, *Phys. Rev. B* **98**, 075439 (2018).
- ⁴⁰J. M. Soler, E. Artacho, J. D. Gale, A. García, J. Junquera, P. Ordejón, and D. Sánchez-Portal, *J. Phys. Condens. Matter* **14**, 2745 (2002).
- ⁴¹D. Sánchez-Portal, P. Ordejón, E. Artacho, and J. M. Soler, *Int. J. Quantum Chem.* **65**, 453 (1997).
- ⁴²E. Artacho, D. Sánchez-Portal, P. Ordejón, A. García, and J. M. Soler, *Phys. Status Solidi B* **215**, 809 (1999).
- ⁴³J. P. Perdew, K. Burke, and M. Ernzerhof, *Phys. Rev. Lett.* **77**, 3865 (1996).
- ⁴⁴N. Troullier and J. L. Martins, *Phys. Rev. B* **43**, 1993 (1991).
- ⁴⁵M. Z. Hossain, T. Ahmed, B. Silverman, M. S. Khawaja, J. Calderon, A. Rutten, and S. Tse, *J. Mech. Phys. Solids* **110**, 118 (2018).
- ⁴⁶L. J. Bartolotti and R. G. Parr, *J. Chem. Phys.* **72**, 1593 (1980).
- ⁴⁷A. Nagy and R. G. Parr, *Phys. Rev. A* **42**, 201 (1990).
- ⁴⁸D. Tsai, *J. Chem. Phys.* **70**, 1375 (1979).
- ⁴⁹R. S. Mulliken, *J. Chem. Phys.* **23**, 1833 (1955).
- ⁵⁰W. Tang, E. Sanville, and G. Henkelman, *J. Phys. Condens. Matter* **21**, 084204 (2009).
- ⁵¹F. L. Hirshfeld, *Theor. Chim. Acta* **44**, 129 (1977).
- ⁵²A. E. Reed, R. B. Weinstock, and F. Weinhold, *J. Chem. Phys.* **83**, 735 (1985).
- ⁵³C. Fonseca Guerra, J.-W. Handgraaf, E. J. Baerends, and F. M. Bickelhaupt, *J. Comput. Chem.* **25**, 189 (2004).
- ⁵⁴M. Segall, R. Shah, C. Pickard, and M. Payne, *Phys. Rev. B* **54**, 16317 (1996).
- ⁵⁵D. A. Penchoff, C. C. Peterson, M. S. Quint, J. D. Auxier, G. K. Schweitzer, D. M. Jenkins, R. J. Harrison, and H. L. Hall, *ACS Omega* **3**, 14127 (2018).
- ⁵⁶L. Zhang, Y. Xie, T. Cui, Y. Li, Z. He, Y. Ma, and G. Zou, *Phys. Rev. B* **74**, 184519 (2006).
- ⁵⁷F. Gao, *Phys. Rev. B* **73**, 132104 (2006).
- ⁵⁸A. Kokalj, *Comp. Mater. Sci.* **28**, 155 (2003).
- ⁵⁹K. Momma and F. Izumi, *J. Appl. Crystallogr.* **41**, 653 (2008).
- ⁶⁰A. Stukowski, *Model. Simul. Mater. Sci. Eng.* **18**, 015012 (2009).
- ⁶¹A. W. Robertson, G.-D. Lee, K. He, E. Yoon, A. I. Kirkland, and J. H. Warner, *Nano Lett.* **14**, 3972 (2014).